

Quantum simulation of the SU(3) Haldane phase with spinor bosons in optical lattices

Junjun Xu*

*Beijing Weak Magnetic Detection and Applied Engineering Technology Research Center,
School of Mathematics and Physics, University of Science and Technology Beijing, Beijing 100083, China and
Institute of Theoretical Physics, University of Science and Technology Beijing, Beijing 100083, China*

(Dated: July 23, 2025)

The Haldane phase with local SU(3) adjoint representation constitutes the simplest non-trivial symmetry-protected topological phases in the SU($N > 2$) Heisenberg spin chains. In this paper, we propose a quantum simulation of this phase using a two-species spinor Bose gas. The system consists of two interlaced, species-dependent zigzag optical lattices, where the two species label the quark and antiquark states of SU(3) symmetry. In the strong-coupling limit, we determine the ground-state phase diagram, and identify a quantum phase transition from the Haldane phase to a dimer phase. We characterize the Haldane phase through its experimental signatures, including edge modes, nonlocal string order, and entanglement spectra. To further understand these observations at the dimer phase, we construct an explicit ground-state ansatz at the dimer point.

I. INTRODUCTION

The Haldane conjecture, which predicts a gapped ground state in antiferromagnetic Heisenberg (AFH) chains with local SU(2) integer-spin representations [1–3], has reshaped our understanding and classification of quantum matters, and leads to the discovery of the symmetry-protected topological (SPT) phases [4–6]. Recently, theoretical progress in this direction generalizes the Haldane conjecture to SU(N) AFH spin chains, and finds a gapless ground state when the number of boxes in the Young diagram p is coprime with N , which is connected to the SU(N)₁ Wess-Zumino-Witten conformal field theory, while for other representations field theory calculations predict a finite mass gap [7–9]. Interpretations about this mass gap include the existence of spinon confinement [10–12], and more recently the fractional topological excitations called instantons [13].

Compared to the SU(2) case, the richer representations of the SU(N) symmetry are predicted to support new features in their gapped states. For example, the SPT phases in SU(N) AFH spin chains can be protected by the $Z_N \times Z_N$ symmetry, and have $N - 1$ distinct non-trivial classes [14–17], corresponding to different elements of the second cohomology group $H^2(Z_N \times Z_N, U(1)) = Z_N$, which can be revealed by the representations of different edge states [18, 19]. At the same time, the ground state of the SU(N) system can have degeneracies if these non-trivial classes are symmetrically connected.

On the numerical front, the minimal model to check above new features is to consider the SU(3) symmetry. For the symmetric representation with Young diagram [3 0 0], large-scale density matrix renormalization group (DMRG) results have recently determined the ground state energy gap to be around $0.04J$ [20]. However, this SPT state is found to be trivial [21], which is confirmed more recently by tensor-network calculations

[22]. For non-symmetric representations, recent Monte Carlo simulations together with field theory calculations show there is always a gapped phase in the SU(3) self-conjugate representations [23], where different from the SU(2) case, the flavor-wave calculation shows six Goldstone bosons with two different velocities, and the topological angle becomes non-trivial with a spontaneously broken parity symmetry for an odd number of boxes.

Thus, the simplest representation in SU(3) symmetry with non-trivial topological properties would be the adjoint representation [2 1 0]. In this system, the edge states of the two sides can be in the representation [1 0 0]–[1 1 0] or [1 1 0]–[1 0 0], corresponding to the two classes of SPT phases, where each class breaks the inversion symmetry, and has different chiralities [24–26]. The Affleck-Kennedy-Lieb-Tasaki (AKLT) state and its parent Hamiltonian have been constructed [10, 11, 27], and this system is found protected by the $Z_3 \times Z_3$ symmetry with a doubly degenerate ground state [18].

On the experimental front, the cold atomic system has become a promising candidate for realizing various SPT phases in their SU(2) representations [28, 29]. For their SU(N) counterparts, progress has been pushed forward to the alkali-earth atomic systems, as a natural emergence of SU(N) symmetry by their nuclear spins [30]. Since all the experimentally accessible spinful alkali-earth atoms are fermionic, proposals in this system are focusing on the fermionic SPT phases with local SU(N) symmetry [31–34], where most cases are with N even and a unique ground state.

In this work, we take on an alternative route by considering a bosonic system, and give in the bosonic system the first experimental proposal for simulating the non-trivial Haldane phase in the SU(3) adjoint representation. This includes mapping the system to a Schwinger bosons representation, and implements a system with two species of bosons a and b , both in three substates of their hyperfine spin $F = 2$ state.

This paper is organized as follows. We first give our mapping from the SU(3) AFH chain with adjoint representation to the spinor Bose gases in Sec. II. In

* jxu@ustb.edu.cn

Sec. III we show the experimental setup to realize such a model, which consists of two interlaced, species-dependent zigzag optical lattices. In Sec. IV we explain its characteristic phases, and determine the ground-state phase diagram by calculating its string order and dimer order. In Sec. V we discuss the experimental observations of the Haldane phase, by calculating its edge modes, nonlocal string order, and entanglement spectra. To understand the above observations in the dimer phase, we further give an explicit ground-state ansatz at the dimer point in Sec. VI. In the end, we give our summaries and outlooks.

II. THE BOSONIC MAPPING

We first show how to map the SU(3) AFH chain with local adjoint representation to a bosonic model, starting from the Hamiltonian [35]

$$H_S = 2 \sum_{\langle ij \rangle, m} T_i^m T_j^m, \quad (1)$$

where T_i^m is the m -th generator ($m=1,2,\dots,8$) of the SU(3) adjoint representation at site i .

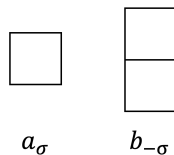


FIG. 1. Two sets of Schwinger bosons that label the fundamental representation of SU(3) symmetry (shown as their corresponding Young diagrams). Three different internal hyperfine states ($\sigma = 2, -2, 0$ as illustrated in Fig. 2c of each boson a_σ and b_σ are included to construct the triplet (quark) and antitriplet (antiquark) representations.

Unlike fermionic systems, there is no way to build antisymmetric representations from Schwinger bosons [11]. Instead, here we use two sets of Schwinger bosons to label the SU(3) fundamental representations as in Fig. 1. Then the generators of any SU(3) irreducible representation can be constructed by these two sets of bosons a and b (the quark and antiquark states) as [36–38]

$$T^m = \frac{1}{2} \sum_{\sigma\sigma'} \left(a_\sigma^\dagger \lambda_{\sigma\sigma'}^m a_{\sigma'} + b_{-\sigma}^\dagger \bar{\lambda}_{\sigma\sigma'}^m b_{-\sigma'} \right), \quad (2)$$

with $\sigma = 2, -2, 0$ as illustrated in Fig. 1, where λ^m are the Gell-Mann matrices that account for the matrix rep-

resentation of a single quark as

$$\begin{aligned} \lambda^1 &= \begin{pmatrix} 0 & 1 & 0 \\ 1 & 0 & 0 \\ 0 & 0 & 0 \end{pmatrix}, \lambda^2 = \begin{pmatrix} 0 & -i & 0 \\ i & 0 & 0 \\ 0 & 0 & 0 \end{pmatrix}, \lambda^3 = \begin{pmatrix} 1 & 0 & 0 \\ 0 & -1 & 0 \\ 0 & 0 & 0 \end{pmatrix}, \\ \lambda^4 &= \begin{pmatrix} 0 & 0 & 1 \\ 0 & 0 & 0 \\ 1 & 0 & 0 \end{pmatrix}, \lambda^5 = \begin{pmatrix} 0 & 0 & -i \\ 0 & 0 & 0 \\ i & 0 & 0 \end{pmatrix}, \lambda^6 = \begin{pmatrix} 0 & 0 & 0 \\ 0 & 0 & 1 \\ 0 & 1 & 0 \end{pmatrix}, \\ \lambda^7 &= \begin{pmatrix} 0 & 0 & 0 \\ 0 & 0 & -i \\ 0 & i & 0 \end{pmatrix}, \lambda^8 = \frac{1}{\sqrt{3}} \begin{pmatrix} 1 & 0 & 0 \\ 0 & 1 & 0 \\ 0 & 0 & -2 \end{pmatrix}, \end{aligned} \quad (3)$$

and for the antiquark $\bar{\lambda}^m = -(\lambda^m)^*$. The Casimirs

$$n_a = \sum_{\sigma} a_{\sigma}^{\dagger} a_{\sigma}, n_b = \sum_{\sigma} b_{\sigma}^{\dagger} b_{\sigma} \quad (4)$$

define the number of quarks and antiquarks in this representation Eq. (2), and determines the dimension of this representation.

At first sight, for $n_a = n_b = 1$ Eq. (2) seems trivially equivalent to the direct product of two independent quark and antiquark representations, and thus the same as a two-leg SU(3) spin chain model with fundamental and antifundamental representations on each leg. We prove that different from this two-leg spin chain model, in fact the generator Eq. (2) naturally projects out the singlet state, and leads to exactly the adjoint representation of SU(3) symmetry.

To see this, we write out the singlet state in terms of our bosonic space

$$|S\rangle = \frac{1}{\sqrt{3}} \sum_{\sigma} a_{\sigma}^{\dagger} b_{-\sigma}^{\dagger} |vac\rangle. \quad (5)$$

The generator Eq. (2) acting on the singlet state gives

$$\begin{aligned} T^m |S\rangle &= \frac{1}{2\sqrt{3}} \sum_{\sigma\sigma'\sigma''} \left(a_{\sigma}^{\dagger} \lambda_{\sigma\sigma'}^m a_{\sigma'} + b_{-\sigma}^{\dagger} \bar{\lambda}_{\sigma\sigma'}^m b_{-\sigma'} \right) a_{\sigma''}^{\dagger} b_{-\sigma''}^{\dagger} |vac\rangle \\ &= \frac{1}{2\sqrt{3}} \sum_{\sigma\sigma'} \left(a_{\sigma}^{\dagger} \lambda_{\sigma\sigma'}^m b_{-\sigma'}^{\dagger} + b_{-\sigma}^{\dagger} \bar{\lambda}_{\sigma\sigma'}^m a_{\sigma'}^{\dagger} \right) |vac\rangle \\ &= \frac{1}{2\sqrt{3}} \sum_{\sigma\sigma'} a_{\sigma}^{\dagger} (\lambda_{\sigma\sigma'}^m + \bar{\lambda}_{\sigma'\sigma}^m) b_{-\sigma'}^{\dagger} |vac\rangle \\ &= \frac{1}{2\sqrt{3}} \sum_{\sigma\sigma'} a_{\sigma}^{\dagger} (\lambda^m + (\bar{\lambda}^m)^T)_{\sigma\sigma'} b_{-\sigma'}^{\dagger} |vac\rangle \\ &= 0, \end{aligned} \quad (6)$$

which means that the generator T^m projects out the singlet state, and there is no matrix element that couples the higher-dimensional representations to the singlet state. Thus for Casimirs $n_a = n_b = 1$, our generator T^m gives exactly the adjoint representation of SU(3) symmetry.

Under this representation, the SU(3) AFH spin chain becomes

$$H_S = \sum_{\langle ij \rangle} H_{ij}^{aa} + H_{ij}^{ab} + H_{ij}^{ba} + H_{ij}^{bb}, \quad (7)$$

with

$$\begin{aligned}
H_{ij}^{aa} &= 1/2 \sum_{\sigma_i \sigma'_i \sigma_j \sigma'_j, m} a_{i, \sigma_i}^\dagger a_{j, \sigma_j}^\dagger a_{j, \sigma'_j} a_{i, \sigma'_i} \lambda_{\sigma_i \sigma'_i}^m \lambda_{\sigma_j \sigma'_j}^m, \\
H_{ij}^{ab} &= 1/2 \sum_{\sigma_i \sigma'_i \sigma_j \sigma'_j, m} a_{i, \sigma_i}^\dagger b_{j, \sigma_j}^\dagger b_{j, \sigma'_j} a_{i, \sigma'_i} \lambda_{\sigma_i \sigma'_i}^m \tilde{\lambda}_{\sigma_j \sigma'_j}^m, \\
H_{ij}^{ba} &= 1/2 \sum_{\sigma_i \sigma'_i \sigma_j \sigma'_j, m} b_{i, \sigma_i}^\dagger a_{j, \sigma_j}^\dagger a_{j, \sigma'_j} b_{i, \sigma'_i} \tilde{\lambda}_{\sigma_i \sigma'_i}^m \lambda_{\sigma_j \sigma'_j}^m, \\
H_{ij}^{bb} &= 1/2 \sum_{\sigma_i \sigma'_i \sigma_j \sigma'_j, m} b_{i, \sigma_i}^\dagger b_{j, \sigma_j}^\dagger b_{j, \sigma'_j} b_{i, \sigma'_i} \tilde{\lambda}_{\sigma_i \sigma'_i}^m \tilde{\lambda}_{\sigma_j \sigma'_j}^m.
\end{aligned}$$

Carrying out the summation over different matrix indices, we have

$$\begin{aligned}
H_{ij}^{aa} &= \left(a_{i,2}^\dagger a_{j,-2}^\dagger a_{j,2} a_{i,-2} + a_{i,2}^\dagger a_{j,0}^\dagger a_{j,2} a_{i,0} + a_{i,-2}^\dagger a_{j,0}^\dagger a_{j,-2} a_{i,0} + \text{H.c.} \right) \\
&+ \frac{1}{2} (n_{a_{i,2}} - n_{a_{i,-2}}) (n_{a_{j,2}} - n_{a_{j,-2}}) + \frac{1}{6} (n_{a_{i,2}} + n_{a_{i,-2}} - 2n_{a_{i,0}}) (n_{a_{j,2}} + n_{a_{j,-2}} - 2n_{a_{j,0}}) \\
&= \left(a_{i,2}^\dagger a_{j,-2}^\dagger a_{j,2} a_{i,-2} + a_{i,2}^\dagger a_{j,0}^\dagger a_{j,2} a_{i,0} + a_{i,-2}^\dagger a_{j,0}^\dagger a_{j,-2} a_{i,0} + \text{H.c.} \right) + n_{a_{i,2}} n_{a_{j,2}} + n_{a_{i,-2}} n_{a_{j,-2}} + n_{a_{i,0}} n_{a_{j,0}} - \frac{1}{3} \\
&= \sum_{\sigma \sigma'} a_{i,\sigma}^\dagger a_{j,\sigma'}^\dagger a_{j,\sigma} a_{i,\sigma'} - \frac{1}{3}, \tag{8}
\end{aligned}$$

$$\begin{aligned}
H_{ij}^{ab} &= - \left(a_{i,2}^\dagger b_{j,-2}^\dagger b_{j,2} a_{i,-2} + a_{i,2}^\dagger b_{j,-2}^\dagger b_{j,0} a_{i,0} + a_{i,-2}^\dagger b_{j,2}^\dagger b_{j,0} a_{i,0} + \text{H.c.} \right) \\
&- \frac{1}{2} (n_{a_{i,2}} - n_{a_{i,-2}}) (n_{b_{j,-2}} - n_{b_{j,2}}) - \frac{1}{6} (n_{a_{i,2}} + n_{a_{i,-2}} - 2n_{a_{i,0}}) (n_{b_{j,-2}} + n_{b_{j,2}} - 2n_{b_{j,0}}) \\
&= - \left(a_{i,2}^\dagger b_{j,-2}^\dagger b_{j,2} a_{i,-2} + a_{i,2}^\dagger b_{j,-2}^\dagger b_{j,0} a_{i,0} + a_{i,-2}^\dagger b_{j,2}^\dagger b_{j,0} a_{i,0} + \text{H.c.} \right) - n_{a_{i,2}} n_{b_{j,-2}} - n_{a_{i,-2}} n_{b_{j,2}} - n_{a_{i,0}} n_{b_{j,0}} + \frac{1}{3} \\
&= - \sum_{\sigma \sigma'} a_{i,\sigma}^\dagger b_{j,-\sigma}^\dagger b_{j,-\sigma'} a_{i,\sigma'} + \frac{1}{3}. \tag{9}
\end{aligned}$$

Note that in deriving the above equations we have taken the strong-coupling limit that each site has only a single a and b boson. Similarly, for the remaining two terms we have

$$H_{ij}^{ba} = - \sum_{\sigma \sigma'} b_{i,\sigma}^\dagger a_{j,-\sigma}^\dagger a_{j,-\sigma'} b_{i,\sigma'} + \frac{1}{3}, \tag{10}$$

$$H_{ij}^{bb} = \sum_{\sigma \sigma'} b_{i,\sigma}^\dagger b_{j,\sigma'}^\dagger b_{j,\sigma} b_{i,\sigma'} - \frac{1}{3}. \tag{11}$$

Plugging these terms into Eq. (7) we then map the SU(3) AFH chain with adjoint representation to the following spin-2 bosonic model

$$\begin{aligned}
H_S &= \sum_{\langle ij \rangle, \sigma \sigma'} \left(a_{i,\sigma}^\dagger a_{j,\sigma'}^\dagger a_{j,\sigma} a_{i,\sigma'} + b_{i,\sigma}^\dagger b_{j,\sigma'}^\dagger b_{j,\sigma} b_{i,\sigma'} \right. \\
&\left. - a_{i,\sigma}^\dagger b_{j,-\sigma}^\dagger b_{j,-\sigma'} a_{i,\sigma'} - b_{i,\sigma}^\dagger a_{j,-\sigma}^\dagger a_{j,-\sigma'} b_{i,\sigma'} \right). \tag{12}
\end{aligned}$$

III. THE EXPERIMENTAL SETUP

To connect with the experiment, we consider a more general Hamiltonian

$$\begin{aligned}
H &= \sum_{\langle ij \rangle, \sigma \sigma'} \left[t \left(a_{i,\sigma}^\dagger a_{j,\sigma'}^\dagger a_{j,\sigma} a_{i,\sigma'} + b_{i,\sigma}^\dagger b_{j,\sigma'}^\dagger b_{j,\sigma} b_{i,\sigma'} \right) \right. \\
&\left. - g_0 \left(a_{i,\sigma}^\dagger b_{j,-\sigma}^\dagger b_{j,-\sigma'} a_{i,\sigma'} + b_{i,-\sigma}^\dagger a_{j,\sigma}^\dagger a_{j,\sigma'} b_{i,-\sigma'} \right) \right], \tag{13}
\end{aligned}$$

where the summation is over the nearest sites and σ corresponds to different hyperfine states. It's obvious that the SU(3) AFH model corresponds to the Heisenberg point with $t = g_0 = 1$. Here the positive intraspecies interaction t accounts for the suppression of hopping for the quarks or antiquarks on the nearest sites, which will be explained in the following. The g_0 term comes from the scattering at total hyperfine spin $F = 0$ channel, which keeps the quark-antiquark pair in the singlet space with $[1 \ 1 \ 1] = \sum_{\sigma} 1/\sqrt{3} a_{\sigma}^\dagger b_{-\sigma}^\dagger |vac\rangle$. Here the spin-2 bosons are crucial, as the Clebsch-Gordon coefficients for two

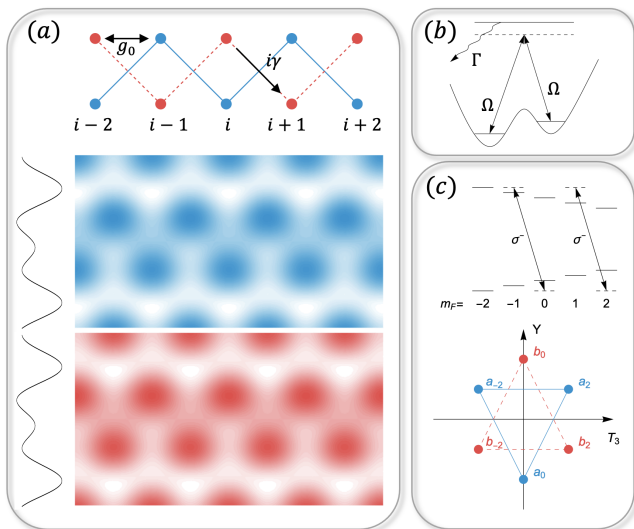


FIG. 2. An illustration of the experimental implementation. (a) The species-dependent optical potential is used to construct two interlaced zigzag lattices, where each species is composed of three degenerate states in the hyperfine $F = 2$ state. The hopping in each species is imaginary $i\gamma$, and the interspecies interaction strength g_0 depends on the overlap of their distribution that is on the same leg. (b) The effective imaginary hopping can be induced by a two-photon Raman process, which couples the states in the tilted lattice to a higher energy level with a decay rate Γ . (c) By combining the magnetic field and σ^- polarized lasers, the three lowest hyperfine states in the spin-2 bosons a and b are picked up, realizing the quark and antiquark representations of the $SU(3)$ symmetry.

spin-1 atoms will lead to a sign change for different scattering states [39], which will break this quark-antiquark singlet state. To reach this Hamiltonian, we need to tune the interaction to be within the strong-coupling limit at filling $n = 1$ for each species [40], and without the interspecies scattering other than total $F = 0$ channel. These could be realized by using optical or microwave Feshbach resonances [41–43].

The experimental setup can be illustrated in Fig. 2. We create a species-dependent zigzag optical lattice by combining the use of lasers with three different wavelengths λ_0 which is blue detuned from species a and red detuned from species b , $\lambda_r = \sqrt{2}\lambda_0$ which is red detuned from the two species, and $\lambda_b = \lambda_0/\sqrt{2}$ which is blue detuned from the two species [44–46]. Two sets of counter propagating λ_0 lasers create a species dependent diagonal square optical lattice $V_{dep} = V_0 \cos(\frac{k_0 x + k_0 y}{\sqrt{2}})^2 + V_0 \cos(\frac{k_0 x - k_0 y}{\sqrt{2}})^2$ with $k_0 = 2\pi/\lambda_0$. A periodic modulation is added along the y axis to separate each two-leg system and reduce the interspecies spin-mixing interaction at the same site with $V_y = V_0 \cos(k_b y + \pi/2 + \phi)^2 - V_0 \cos(k_r y + \pi/4)^2$, as illustrated in the solid curve in Fig. 2a, where we have added a small phase difference ϕ to create a tilted lattice [47–49]. A demonstration of the realized species-dependent optical lattice for atoms a (blue) and b (red) is shown in

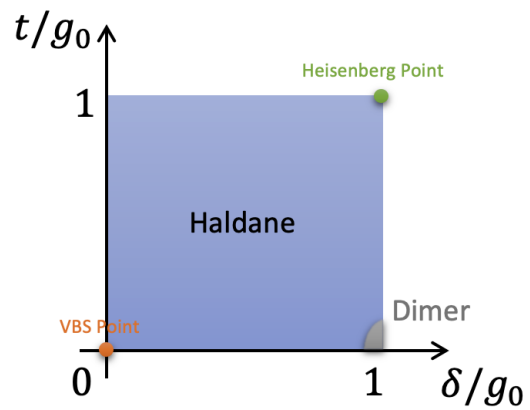


FIG. 3. Characteristic phase diagram in our parameter regime. The Heisenberg limit and VBS limit in the Haldane phase are shown as the green and orange points. As explained in the Appendix, the experimentally accessible regime is for t positive. The regime at $\delta/g_0 > 1$ is not shown, as it corresponds to its inverse chiral counterpart, and the phase diagram is symmetric along the line $\delta = g_0$.

Fig. 2a, where the denser color corresponds to a lower trap depth. Here the tilted lattices prevent the hopping of atoms at the nearest sites within each species, and at the same time help to include an effective imaginary hopping. We propose to use two Raman lasers with Rabi frequency Ω to couple the tilted lattices to the same higher energy level which has a decay rate Γ as in Fig. 2b. The detuning and decay rate can be tuned to be sufficiently large so that by adiabatic elimination we end up with an imaginary hopping $i\gamma \propto i\Omega^2/\Gamma$ in the zig-zag lattice as in Fig. 2a. By a non-Hermitian perturbation theory [50], this imaginary hopping gives rise to a positive interaction t in Eq. (13). To realize a $SU(3)$ symmetric system within the hyperfine spin $F = 2$ states, we propose to combine the magnetic field with σ^- polarized lasers to pick up the lowest hyperfine states with $m_F = 0, \pm 2$ as shown in Fig. 2c. In this case, we can map these lowest hyperfine states a_σ and b_σ to the quark and antiquark states.

IV. THE PHASE DIAGRAM

We show in Fig. 3 the characteristic phase diagram in the parameter regime at the strong-coupling limit. To illustrate the evolution to the $SU(3)$ chiral Haldane phase, we include an energy shift δ to the left and right chiral states in the interspecies interaction with $-\sum_{\langle ij \rangle, \sigma\sigma'} \left(g_0 a_{i,\sigma}^\dagger b_{j,-\sigma}^\dagger b_{j,-\sigma'} a_{i,\sigma'} + \delta b_{i,-\sigma}^\dagger a_{j,\sigma}^\dagger a_{j,\sigma'} b_{i,-\sigma'} \right)$, where $j > i$ and $\delta/g_0 \in [0, 1]$. This corresponds to a shift of these two species-dependent optical lattices in the experiment, and can be realized by including an additional trap along the x axis. As expected, a well-defined valence bond solid (VBS) state (orange) is found at the

point $t = \delta = 0$ where a right chiral SU(3) singlet pair is formed at nearest sites. By increasing t and δ the system can adiabatically evolve to the Heisenberg point (green) with $t = \delta = g_0$, where the Haldane phase shows double degeneracy of the left and right chiral states. As will be explained later, by decreasing t from the Heisenberg point, the Haldane phase will become unstable, and there will be a phase transition to a dimer phase (gray).

To confirm the above qualitative phase diagram in Fig. 3, we consider the following string order parameter in the Schwinger bosons representation

$$C^{\text{Str}}(i, j) = \left\langle \Delta n_2^i e^{i\pi \sum_{i < k < j} \Delta n_2^k} \Delta n_2^j \right\rangle, \quad (14)$$

where $\Delta n_2^i = n_{a_2}^i - n_{b_{-2}}^i$ measures the particle number difference between the quark and antiquark state a_2 and b_{-2} at site i . This number difference corresponds to the charge $Q^i = \Delta n_2^i = T_3^i + Y^i/2$ according to the Gell-Mann-Nishijima formula, and thus takes values $-1, 0$, and 1 in the meson state [51, 52], where

$$T^3 = \frac{1}{2} (n_{a_2} - n_{a_{-2}}) + \frac{1}{2} (n_{b_2} - n_{b_{-2}}), \quad (15)$$

$$\begin{aligned} Y &= \frac{1}{3} (n_{a_2} + n_{a_{-2}} - 2n_{a_0}) + \frac{1}{3} (2n_{b_0} - n_{b_2} - n_{b_{-2}}) \\ &= \frac{1}{3} (3n_{a_2} + 3n_{a_{-2}} - 2) + \frac{1}{3} (2 - 3n_{b_2} - 3n_{b_{-2}}) \\ &= n_{a_2} + n_{a_{-2}} - n_{b_2} - n_{b_{-2}}. \end{aligned} \quad (16)$$

We note the string order we define here is similar to the one by Morimoto *et al.* [18], and different from [14].

To give the characteristic phase diagram as shown in Fig. 3, we carry out calculations about the string order defined in Eq. (14) with an additional dimer order

$$C^{\text{dim}} = \langle \Delta n_2^{L/2} \Delta n_2^{L/2+1} - \Delta n_2^{L/2} \Delta n_2^{L/2-1} \rangle, \quad (17)$$

which measures the difference of correlations at even and odd bonds. The dimer order C^{dim} can measure the translational symmetry-breaking state that appears in the system.

We consider DMRG calculations with system size $L = 128$ and bond dimension as large as 1600. Our results are summarized in Fig. 4, where the sizes of squares and triangles label the magnitudes of the string and dimer orders respectively. We find there is a rather small regime near the dimer point $t/g_0 = 0, \delta/g_0 = 1.0$ where the system breaks the translational symmetry and goes into a dimer phase. We note a similar phase transition has also been observed in a two-leg SU(3) spin ladder [53]. These results confirm our qualitative phase diagram in Fig. 3.

V. EXPERIMENTAL OBSERVATIONS

In this section, we give experimental signatures of the Haldane phase. In a lattice system, the quantum gas microscope is a powerful technique that can give direct local

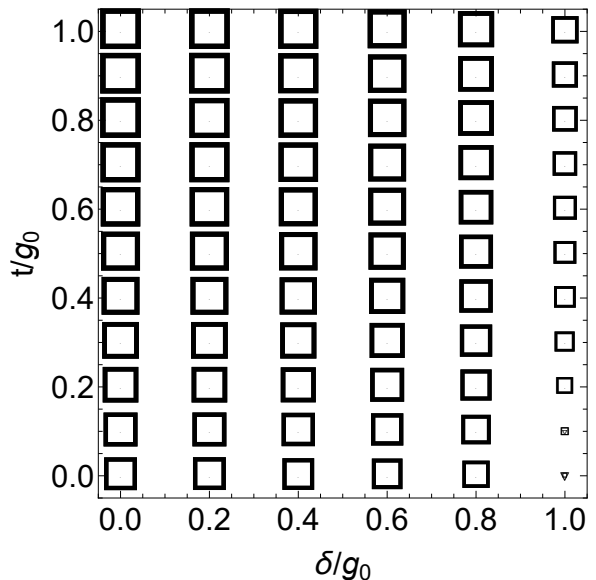


FIG. 4. The order parameters obtained from DMRG calculations with system size $L = 128$. The squares and triangles label the string and dimer orders respectively, with their sizes corresponding to their magnitudes. A translational symmetry-breaking dimer phase is observed at a small regime near the dimer point $t/g_0 = 0, \delta/g_0 = 1.0$.

observations, as well as correlations [54–58]. To connect with the actual experiment, we will focus on a limited lattice size with $L = 16$, and discuss the observations of edge modes, non-local string order, and entanglement spectrum.

A. Edge modes

The most direct confirmation of the Haldane phase would be observing its edge modes. We consider an open chain lattice, and to reduce the Hilbert space and lift up additional degeneracies, we restrict the subspaces to have $T_3 = 1$ and $Y = 0$. This corresponds to post-select the microscopic images with Hilbert space $S_z = 2$ for both a and b particles.

We show the particle number distribution and its corresponding local T_3 and Y for different parameters in Fig. 5. The VBS state in Fig. 5a clearly shows a single particle a_2 and b_2 appear at each edge of the open chain, which signals the quark and antiquark edge modes that appear in the chiral Haldane phase. These edge modes can also be seen from the T_3/Y plot. In Fig. 5b we show the position between VBS and Heisenberg point (HP) at $t/g = \delta/g = 0.5$. We observe the same edge modes that are robust in the Haldane phase.

For the HP in Fig. 5c, we observe different behaviors. The edge modes become weak and we observe two edge a_2 and b_2 modes on both sides. This signals a non-trivial property of the Haldane phase in the SU(3) adjoint representation, that the ground state can support a two-fold

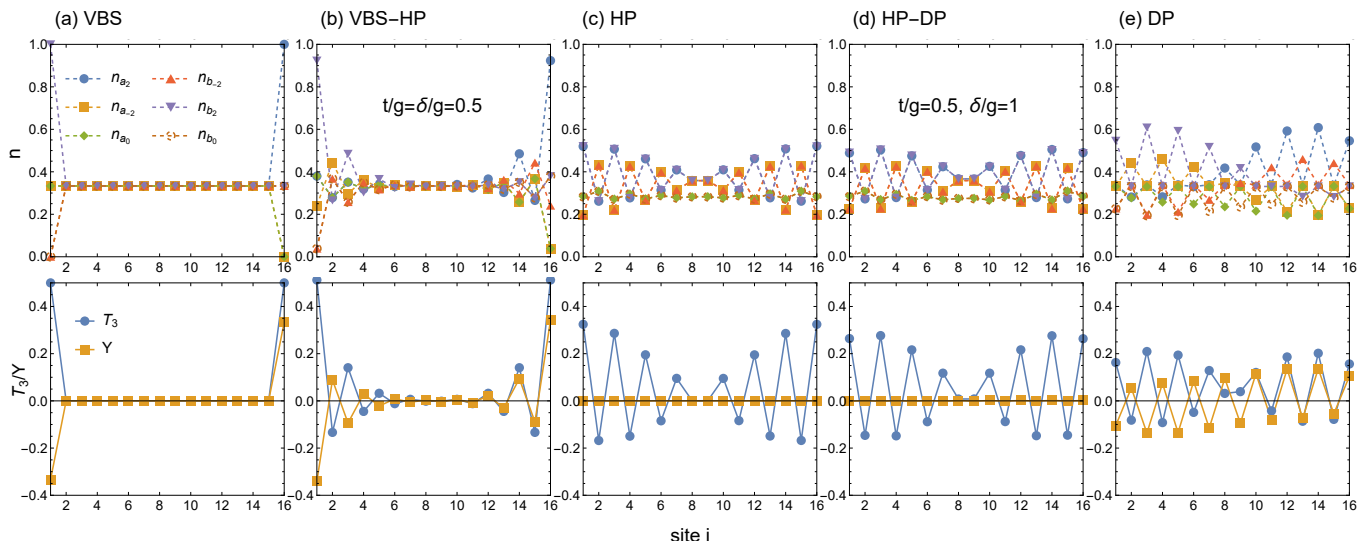


FIG. 5. The local particle number distribution and the corresponding local T_3 and Y for different parameters. From (a) to (e) we are at the VBS point ($t/g = \delta/g = 0$), VBS to Heisenberg point (VBS-HP) ($t/g = \delta/g = 0.5$), Heisenberg point (HP) ($t/g = \delta/g = 1$), Heisenberg to dimer point (HP-DP) ($t/g = 0.5, \delta/g = 1$), and the dimer point (DP) ($t/g = 0, \delta/g = 1$). The edge modes can be clearly seen in both VBS and VBS-HP, which supports a chiral Haldane phase. In the HP, the Haldane phase shows two-fold degeneracy, and as a result the particle distribution shows edge modes of two different chiral states, and in the same sense, the local Y cancels to zero due to the superposition of these two chiral Haldane phases. The HP-DP in (d) is close to the transition, as the edge modes become weaker. However, since the local Y is still homogeneous and the double degeneracy is conserved, this state is closer to the Haldane phase. In (e) we observe a spontaneous breaking of lattice translational symmetry from the local Y , and thus this state belongs to a trivial dimer phase, with the double degeneracy in particle distribution also broken.

degeneracy. The superposition of these two degenerate ground states with opposite chiralities leads to the cancellation of local Y as illustrated in Fig. 5c, while the edge modes are more visible from the local T_3 plot. The decay of edge modes as a function of sites becomes slower, indicating a smaller energy gap at the HP.

At the HP to dimer point (DP) in Fig. 5d for $t/g = 0.5$ and $\delta/g = 1$, these edge modes are even weaker, and the system is close to a transition to the dimer phase. However, the Y plot still shows a translational symmetry, indicating that the system is closer to a Haldane phase. At the DP in Fig. 5e, we observe a spontaneous breaking of lattice translational symmetry from the Y plot, and the system is in a trivial dimer phase, where the doubly degenerate edge modes are also lost from the local particle density.

B. String order

The experimental observation of string order is within the current cold atoms techniques. However, the system sizes should be very limited. We show this string order parameter for different intraspecies interaction t and interspecies spin-mixing energy shift δ for an experimentally realizable system size $L = 16$ in Fig. 6a by DMRG calculations. As previously, we consider an open system, and choose subspaces with $T_3 = 1$ and $Y = 0$. We

observe a finite string order all through our parameter regime, and find it decreases apparently close to $\delta/g_0 = 1$ and $t = 0$, which is consistent with the existence of a quantum phase transition near this point at the thermodynamic limit.

We note that due to the small system size in the experiment, it is unlikely to observe the transition to a dimer phase from the string order. We further push the DMRG calculations all through to system size $L = 128$ and keep up to 1600 states at the dimer point, the string order parameter shows a power-law behavior as in Fig. 6b, in contrast to the exponential behavior as expected for a gapped dimer phase. We attribute this to our selection of subspaces that rules out the dimer ground state (see the Appendix).

C. Entanglement spectrum

The experimental observation of the entanglement spectrum might still be challenging, however it provides a more robust test to symmetry-protected states [5]. We illustrate the evolution of the entanglement spectrum in Fig. 7 from the VBS and Heisenberg points to the dimer point. To avoid boundary effects, here we consider a periodic chain and take an experimentally accessible chain length $L = 16$.

The entanglement spectrum shows a well-defined 9-

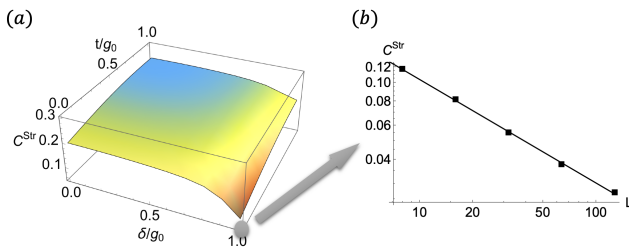


FIG. 6. (a) The string order parameter $C^{\text{Str}} = C^{\text{Str}}(L/4, 3L/4)$ as a function of intraspecies interaction t and interspecies spin-mixing energy shift δ . (b) Finite-size scaling of the string order parameter shows a power-law behavior at the dimer point for $t/g_0 = 0$ and $\delta/g_0 = 1$.

fold degeneracy in the VBS point (orange) in Fig. 7a, corresponding to the entanglement of two fundamental SU(3) edge modes (quark or antiquark states) with each of which appears at one boundary of the half system. This degeneracy clearly reveals the appearance of the chiral Haldane phase. Besides this, we also observe a very large entanglement gap above the ninth entanglement eigenvalue in the Haldane phase. Close to the dimer phase (gray) around $t/g_0 = 0$ and $\delta/g_0 = 1$, the 9-fold degeneracy is lifted up with this entanglement gap vanishing. The closing of this entanglement gap has an intuitive explanation. As the system goes into a trivial state, the edge modes can only support representations with integer numbers of Young diagram boxes, so the lowest entanglement eigenvalue would be one singlet at each boundary and unique, and the second lowest entanglement eigenvalues would be a singlet and an octet at each boundary with a total 16-fold degeneracy. This gives a closing of the entanglement gap above the ninth entanglement eigenvalue and signals the appearance of a trivial state.

As illustrated in Fig. 7b, deviated from the dimer phase the entanglement gap above the ninth entanglement eigenvalue reopens, and the nine smallest entanglement eigenvalues gather when approaching the Heisenberg point (green). Here we note our DMRG calculations naturally search for one of the two degenerate chiral ground states in the Heisenberg point, with the lowest entanglement spectrum showing 9-fold (instead of 18-fold) degeneracy approaching the thermodynamic limit. In contrast to the VBS point, the Heisenberg point suffers much from the finite-size effect and shows an absence of the 9-fold degeneracy in its lowest entanglement eigenvalues. This finite-size effect is similar to the spin-1 Haldane phase, and is due to the spectrum gap between the SU(3) singlet state and 8-fold octet states formed by the two SU(3) fundamental representations appearing at the edges. We also find that the entanglement gap above the ninth entanglement eigenvalue is more robust than the 9-fold degeneracy of the lowest entanglement eigenvalues, and suffers little from the finite-size effect.

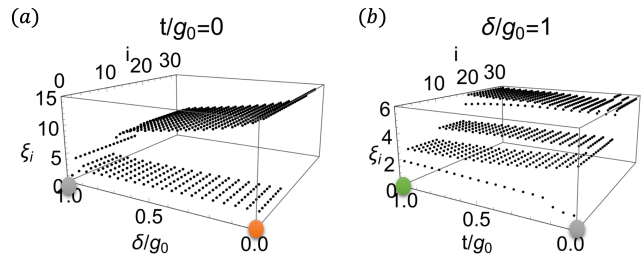


FIG. 7. Evolution of the entanglement spectrum from the VBS to dimer point at $t/g_0 = 0$ in (a) and from the dimer to Heisenberg point at $\delta/g_0 = 1$ in (b). There is a spectrum gap above the 9th entanglement eigenvalue ξ_9 in both the VBS (orange) and Heisenberg (green) points. Approaching the dimer phase (gray) this spectrum gap closes.

VI. A SOLUTION TO THE DIMER POINT

The physics of this dimer phase is not trivial and lacks analytical solutions. To further understand this phase, in this section we focus on the dimer point, and try to construct an analytical ground state ansatz with the following reduced Hamiltonian

$$H_d = - \sum_{\langle ij \rangle, \sigma \sigma'} \left(a_{i,\sigma}^\dagger b_{j,-\sigma}^\dagger b_{j,-\sigma'} a_{i,\sigma'} + b_{i,-\sigma}^\dagger a_{j,\sigma}^\dagger a_{j,\sigma'} b_{i,-\sigma'} \right). \quad (18)$$

We start from the right chiral Haldane phase $|\psi_R\rangle$ as illustrated in the inset of Fig. 8, where the red and blue dots label the quark and antiquark states at site i , and the solid lines label the SU(3) singlet bonds. We observe that if the Hamiltonian H_d is acting on $|\psi_R\rangle$, the resulting states are a superposition of states with each quark/antiquark state connected with a single solid line. So the effects of the Hamiltonian H_d just shift these solid lines. This observation suggests the ground state of H_d might be constructed from states with fully connected singlet states.

We label each substate as $\{|r_i\rangle\}$ with the quark state at site i connected to the antiquark state at site r_i , and different structures correspond to different permutations of the list from 1 to L . For example, the right chiral Haldane phase $|\psi_R\rangle$ can be labeled as $|2, 3, 4, \dots, L, 1\rangle$. The two-site system $L = 2$ is trivial, and the ground state is easily found as the fully connected state $|2, 1\rangle$. In the following, we first give the exact result of a small system size $L = 3$, and then generalize this solution to arbitrary sizes.

For $L = 3$ there are five possible fully connected states, where we have excluded the trivial state $|1, 2, 3\rangle$ as it is decoupled from the right chiral Haldane phase. One can show this by looking at the resulting states starting from the right chiral Haldane phase, and these states should have at least one singlet bond connecting the nearby sites. The ground state can then be expanded using these five

states as

$$|\psi_3\rangle = A_1|3, 2, 1\rangle + A_2|1, 3, 2\rangle + A_3|2, 1, 3\rangle + A_4|2, 3, 1\rangle + A_5|3, 1, 2\rangle. \quad (19)$$

By solving the Schrödinger equation $H_d|\psi_3\rangle = E_3|\psi_3\rangle$ we find the coupled equations for these coefficients

$$\begin{cases} -A_5 - A_4 - 6A_1 = E_3A_1 \\ -A_4 - A_5 - 6A_2 = E_3A_2 \\ -A_4 - A_5 - 6A_3 = E_3A_3 \\ -2A_3 - 2A_2 - 2A_1 - 9A_4 = E_3A_4 \\ -2A_1 - 2A_3 - 2A_2 - 9A_5 = E_3A_5 \end{cases}. \quad (20)$$

Obviously, the above equations have symmetric solutions with $A_1 = A_2 = A_3$ and $A_4 = A_5$, and under this symmetry we find the energy obeys $\frac{2}{E_3+6} = \frac{(E_3+9)}{6}$, which gives us the exact ground state energy $E_3 = -(15 + \sqrt{57})/2$.

We now generalize to length L . Since we take into account the translational invariant of the system and consider the periodic boundary condition, it is more convenient to transform the Hamiltonian into momentum space as

$$H_d = -\frac{2}{L} \sum_{q,k,k',\sigma,\sigma'} \cos(k-k') \times a_{\frac{q}{2}+k,\sigma}^\dagger b_{\frac{q}{2}-k,-\sigma}^\dagger b_{\frac{q}{2}-k',-\sigma'} b_{\frac{q}{2}+k',\sigma'}. \quad (21)$$

Similar to the above $L = 3$ case, the ground state ansatz can be written as

$$\begin{aligned} |\psi\rangle &= \sum_{\{r_i\}} c_{\{r_i\}} |r_1 r_2 \dots\rangle \\ &= \sum_{\{r_i\}} c_{\{r_i\}} \cdot \sum_{k_1,\sigma_1,k'_1,\sigma'_1,\dots} a_{k_1,\sigma_1}^\dagger b_{k'_1,\sigma'_1}^\dagger a_{k_2,\sigma_2}^\dagger b_{k'_2,\sigma'_2}^\dagger \dots \\ &\quad \times e^{i(k_1+k'_1 r_1)} e^{i(2k_2+k'_2 r_2)} \dots |vac\rangle, \end{aligned} \quad (22)$$

where the summation is over all possible configurations of the SU(3) singlet bonds labeled as $\{r_i\}$. The coefficients $c_{\{r_i\}}$ can be determined through

$$\begin{aligned} &H_d |r_1 r_2 \dots\rangle \\ &= -N \sum_i (\delta_{i-r_i-1,0/L} + \delta_{i-r_i+1,0/L}) |\dots r_i \dots\rangle \\ &\quad - \sum_{i \neq j} (\delta_{i-r_j-1,0/L} + \delta_{i-r_j+1,0/L}) |\dots r_j \dots r_i \dots\rangle \\ &= -N \sum_i (\delta_{i-r_i-1,0/L} + \delta_{i-r_i+1,0/L}) |r_1 r_2 \dots\rangle \\ &\quad - \sum_{i \neq j} (\delta_{i-r_j-1,0/L} + \delta_{i-r_j+1,0/L}) |\dots r_j \dots r_i \dots\rangle, \end{aligned}$$

where $N = 3$ for a SU(3) system. Thus we get the coupled

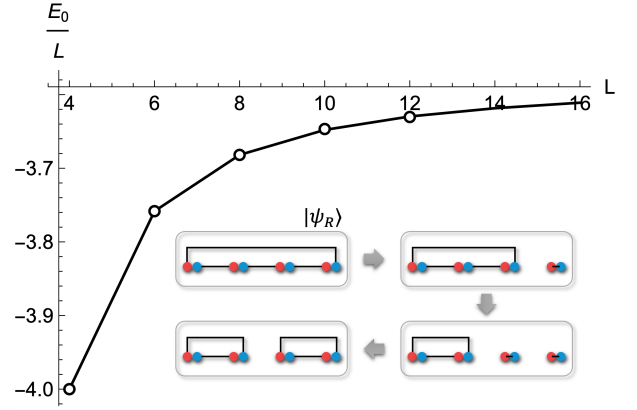


FIG. 8. Ground state energy density E_0/L at the dimer point for different system sizes L . The open points are results from the coupled Eqs. (23), and the solid line shows the DMRG results. The inset illustrates four substates in the ground state of the $L = 4$ system, with blue and red points labeling the quark and antiquark states and solid lines representing the SU(3) singlet bonds.

pled equations for the coefficients

$$\begin{aligned} &E c_{r_1 r_2 \dots} \\ &= -N \sum_i (\delta_{i-r_i-1,0/L} + \delta_{i-r_i+1,0/L}) c_{r_1 r_2 \dots} \\ &\quad - \sum_{i \neq j} (\delta_{i-r_i-1,0/L} + \delta_{i-r_i+1,0/L}) c_{\dots r_j \dots r_i \dots} \\ &= - \sum_{ij} [1 + (N-1) \delta_{ij}] \\ &\quad \times (\delta_{i-r_i-1,0/L} + \delta_{i-r_i+1,0/L}) c_{\dots r_j \dots r_i \dots} \end{aligned} \quad (23)$$

The above coupled equations are huge and hard to solve. For system size L , there are at most $L! - 1$ coefficients to find. However, we can always simplify these equations by the symmetry of the subspaces. For example, similar to the $L = 3$ case, we always have the coefficient of right chiral Haldane phase $|2, 3, 4, \dots, L, 1\rangle$ equals the one of the left chiral Haldane phase $|L, 1, 2, \dots, L-1\rangle$. The coupled equations can then be solved as follows. We start from the left and right chiral Haldane phases with other fully connected states unoccupied. After finding the energy E , we take into account the equations with states coupled with the occupied ones and find the corresponding coefficients. The energy is then updated with new occupied states. This procedure is carried out iteratively until we get the convergent ground-state energy. In Fig. 8 we show the ground state energy densities with above ansatz as the open points, which coincide well with our DMRG results (solid line). This justifies our description at the dimer point.

We can now give a microscopic explanation of the breakdown of the entanglement spectrum degeneracy in the dimer phase. As illustrated in the inset of Fig. 8, the

redistribution of these singlet bonds leads to subspaces which are product states of the left and right subsystems. Occupation of these states lifts the entanglement spectrum degeneracy, and leads this system to a dimer phase. This also explains why the positive t in Eq. (13) is crucial to realize the SU(3) Haldane phase, since this term suppresses the hopping of quark/antiquark states that leads to the product states as shown by the gray arrows in Fig. 8, and thus stabilizes the Haldane phase.

VII. SUMMARY AND OUTLOOK

To conclude, we have proposed an experimentally feasible cold atomic system to realize the non-trivial Haldane phase with local SU(3) symmetry. We show how to construct species-dependent zigzag optical lattices to reach the SU(3) adjoint representation with two spinor Bose gases, and find various experimental signatures to detect the Haldane phase. We identify a phase transition from the Haldane phase to a dimer phase, and explain the break of entanglement spectrum degeneracy at this phase by constructing its ground state wavefunction.

Finally, we mention current experimental techniques. The different edge states of the Haldane phase can be directly observed by quantum gas microscopes, as well as their string order parameters. For example, this technique has been used to observe the edge modes and string order in a two-ladder realization of spin-1 Haldane phase [59]. A Protocol for measuring the entanglement spectrum in cold atomic systems has been proposed [60], however the experimental realization might still be challenging.

Due to the existence of an extremely small energy gap in the SU(3) Haldane phase [20, 22], one might expect the ground state to be very sensitive to the temperature. However, as the experimentally accessible regime could be closer to the VBS point, the excited states will be lifted compared to the Heisenberg point, resulting in a larger energy gap. Another possible way to overcome this is to consider a finite-temperature topology that can detect the non-trivial ground state by means of its thermal ensemble, for example, to measure its ensemble geometrical phase [61, 62].

ACKNOWLEDGEMENTS

This research is supported by the Fundamental Research Funds for the Central Universities (No. FRF-BD-25-033). We would like to thank Philippe Lecheminant, Thomas Quella, and Hosho Katsura for helpful comments.

Appendix A: Realize the imaginary hopping

We propose to use a two-photon Raman process to realize an effective imaginary hopping between tilted lattices as shown in Fig. 9.

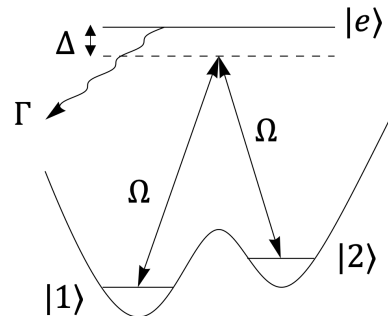


FIG. 9. By coupling the same hyperfine state at the tilted lattice to a higher excited state $|e\rangle$ with a large detuning Δ and decay rate Γ , we end up with an effective imaginary hopping.

For simplicity, let's consider a single particle with the same hyperfine state $m_F = 0, 2$ or -2 at the nearest-neighbor lattice site labeled as $|1\rangle$ and $|2\rangle$, and the excited state $|e\rangle$ has a decay rate Γ and detuning Δ . The Hamiltonian of this two-site system can be written as

$$H_{12} = \Omega(b_1^\dagger b_e + b_2^\dagger b_e + \text{H.c.}) + (\Delta - i\Gamma)b_e^\dagger b_e, \quad (\text{A1})$$

where Ω labels the Rabi frequency of these two Raman lasers. If the excited state has a large detuning and decay rate ($\Delta, \Gamma \gg \Omega$), atomic numbers in this state will quickly decay into a negligible steady value. In this case, we can adiabatically eliminate the excited state by considering the equation of motion

$$\dot{b}_e^\dagger = i[H_{12}, b_e^\dagger] = 0, \quad (\text{A2})$$

which gives

$$b_e^\dagger = -\frac{\Omega}{\Delta - i\Gamma}(b_1^\dagger + b_2^\dagger). \quad (\text{A3})$$

By eliminating the excited state $|e\rangle$ using the above equation, we get an effective Hamiltonian

$$\tilde{H}_{12} = -\frac{\Omega^2}{\Delta - i\Gamma}(n_1 + n_2 + b_1^\dagger b_2 + b_2^\dagger b_1). \quad (\text{A4})$$

We compare this effective Hamiltonian with the original one in Fig. 10, and illustrate the time evolution of different states starting from state $|1\rangle$ at detuning $\Delta/\Omega = 5$ and decay rate $\Gamma/\Omega = 20$. From the dotted points we can find that the above effective Hamiltonian \tilde{H}_{12} gives us a desirable description of the long-time steady state. The appearance of such a steady state is due to the fact that the non-Hermitian system supports a real eigenenergy solution. In this case, a Rayleigh-Schrödinger type

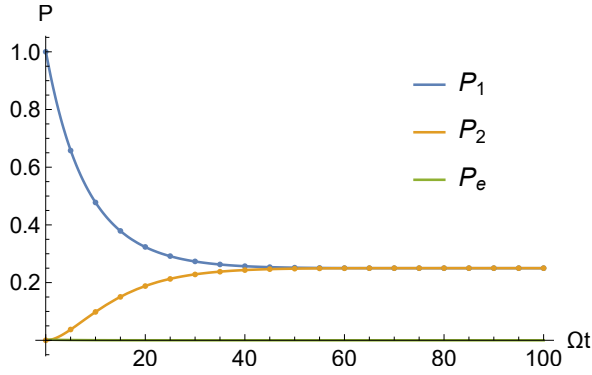


FIG. 10. Probabilities of different states as a function of time starting from state $|1\rangle$. The solid lines show the evolution of Hamiltonian H_{12} , and the points correspond to results from the effective Hamiltonian \tilde{H}_{12} . The detuning and decay rate are chosen as $\Delta/\Omega = 5$ and $\Gamma/\Omega = 20$.

non-Hermitian perturbation theory [50] can be carried out.

Now considering a large decay rate $\Gamma \gg \Delta$, the Hamiltonian \tilde{H}_{12} gives an imaginary hopping $i\gamma = -i\Omega^2/\Gamma$. Then under the non-Hermitian perturbation theory, and taking into account the strong-coupling limit with unit filling that prohibits double occupation at each lattice site, only the double hopping terms support a non-trivial contribution and we arrive at the following effective term

$$H_t = t \sum_{\langle ij \rangle, \sigma\sigma'} \left(a_{i,\sigma}^\dagger a_{j,\sigma'}^\dagger a_{j,\sigma} a_{i,\sigma'} + b_{i,\sigma}^\dagger b_{j,\sigma'}^\dagger b_{j,\sigma} b_{i,\sigma'} \right), \quad (\text{A5})$$

with the positive coefficient $t = \Omega^4/(\Gamma^2 U)$ and U the energy shift for a single hopping.

Appendix B: Determine the energy gap

Determining the energy gap at the dimer point is not trivial. From our ground-state ansatz in the main text, it is reasonable to speculate that there should be an energy gap at the dimer phase, which corresponds to the breaking of a single dimer. However, as mentioned in the experimental signature of the string order, we observe a seemingly critical behavior at this point in Fig. 6, which we attribute to the constraint of Hilbert space that introduces gapless excitations to the system.

Here we confirm that the dimer point is indeed gapped. We first release this constraint and recalculate the string order for various system lengths. We consider system sizes as large as $L = 128$ with the bond dimension as large as $m = 2000$, and illustrate our results in Fig. 11. We show log-linear and log-log plots of the string order C^{Str} for different system sizes in Fig. 11a and b, respectively. For long distances, the string order shows an exponential behavior as guided by the red line in Fig. 11a. This is consistent with a gapped ground state.

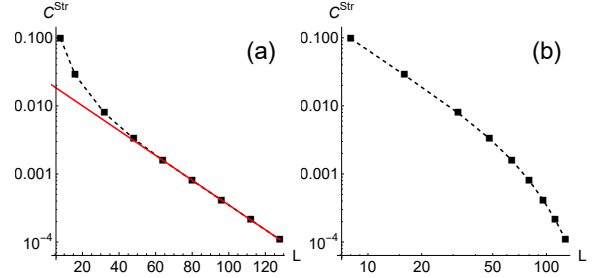


FIG. 11. The (a) log-linear and (b) log-log plot of the ground state string order at the dimer point. The string order shows an exponential behavior at long distances as indicated by the red line in (a), with the fitting giving $C^{Str}(r) = 0.023 \times e^{-0.08r}$.

We then go beyond the ground state string order, and calculate the energy gap for various system sizes as shown in Fig. 12. We do a second-order polynomial fitting to the energy gap as a function of $1/L$ as the dashed line, and determine the energy gap at the dimer point to be around 0.16, which is the same order predicted by the exponential decay in Fig. 11a.

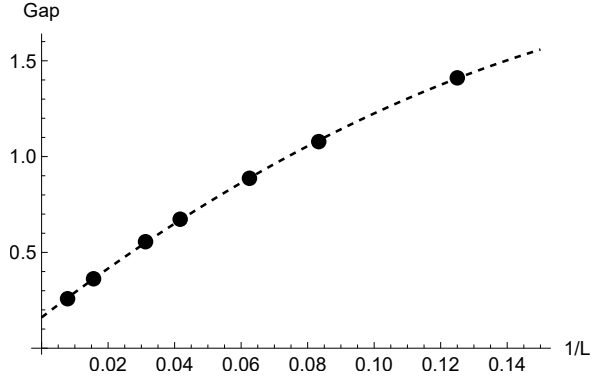


FIG. 12. The energy gap at the dimer point as a function of inverse system size $1/L$. The dashed line corresponds to a second-order polynomial fitting, which coincides well with our numerical results. This fitting gives an energy gap of around 0.16.

Appendix C: The free bond excitations approximation

In the main text, we give exact calculations of the dimer point and explain how the ground state supports the entanglement behavior. However, these exact calculations can only be limited to rather small system sizes. In this appendix, we provide a free bond excitations approximation that neglects the interaction between different excitations. This approximation, though not exact, can be pushed to very large system sizes, and provide an upper limit for the ground state energy of the dimer

point.

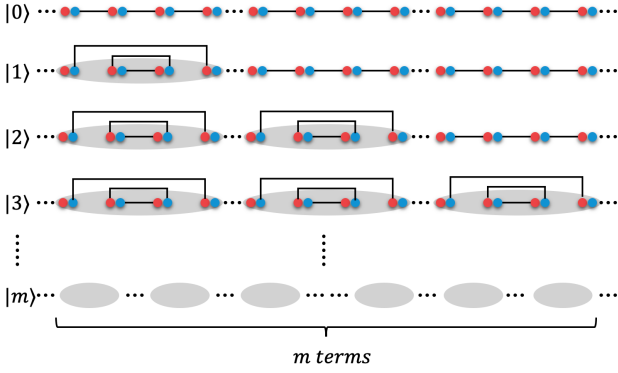


FIG. 13. Illustration of different orders of excited states $|m\rangle$ with m the number of two-bond excitations, starting from a right chiral VBS state. The 1-st order excited state $|1\rangle$ is created by breaking two right chiral singlet bonds and forming two singlets. As the order increases, more and more two-bond excitations are created. In our free bond excitations approximation, we assume that these excitations are dilute and non-interacting. Note that in this illustration we only start from the right chiral state, the same picture also happens in the left chiral configuration, which is also included in our calculations.

We start with the 0-th order state which is the VBS state of left and right chiral as

$$|0\rangle = \left(\prod_i R_i^{i+1} + \prod_i L_i^{i+1} \right) |vac\rangle, \quad (C1)$$

where $R_i^{i+1} = \sum_{\sigma} a_{i,\sigma}^{\dagger} b_{i+1,-\sigma}^{\dagger} / \sqrt{3}$ and $L_i^{i+1} = \sum_{\sigma} b_{i,-\sigma}^{\dagger} a_{i+1,\sigma}^{\dagger} / \sqrt{3}$ are the right and left chiral singlet bond creation operator. Considering the dimer Hamiltonian H_d acting on this 0-th order state, it will create bunches of two-bond excited states as

$$|1\rangle = \sum_i \left(L_i^{i+1} R_{i-1}^{i+2} \prod_{j \neq i \pm 1} R_j^{j+1} + R_i^{i+1} L_{i-1}^{i+2} \prod_{j \neq i \pm 1} L_j^{j+1} \right) |vac\rangle, \quad (C2)$$

and from this state the dimer Hamiltonian can again create an extra excitation to double two-bond excited state $|2\rangle$. More and more excitations can be excited to the system, and we can have different numbers of two-bond excitation states $|n\rangle$ where n labels the number of two-bond excitations.

We illustrate these states excited from the right chiral VBS one in Fig. 13, where we have made an approximation that these two-bond excitations are far from each other, and the interaction between these excitations is negligible. This approximation is reasonable as long as

there is a finite number of excitations that contribute to the system in the thermodynamic limit.

We consider a cutoff m for the excitation number, and the state of the system can be written as a sum of these different excitations

$$|\psi\rangle = \sum_{n=0}^m c_n |n\rangle, \quad (C3)$$

where c_n is the coefficient of state with free excitation number n . Considering the dimer Hamiltonian H_d acting on these states will give

$$\begin{cases} H_d|0\rangle = -3L|0\rangle - |1\rangle \\ H_d|1\rangle = -3(L-1)|1\rangle - 2L|0\rangle - |2\rangle \\ H_d|2\rangle = -3(L-2)|2\rangle - 4(L-1)|1\rangle - |3\rangle \\ \vdots \\ H_d|m\rangle = -3(L-m)|m\rangle - 2m(L-m+1)|m-1\rangle - |m+1\rangle \end{cases},$$

where L is the length of the chain. Given the Schrodinger equation $H_d|\psi\rangle = E|\psi\rangle$ and comparing the coefficients of each state, we arrive at the following iterative equations

$$\begin{cases} EC_0 = -3LC_0 - 2LC_1 \\ EC_1 = -3(L-1)C_1 - 4(L-1)C_2 - C_0 \\ EC_2 = -3(L-2)C_2 - 6(L-2)C_3 - C_1 \\ \vdots \\ EC_m = -3(L-m)C_m - 2(m+1)(L-m)C_{m+1} - C_{m-1} \end{cases}.$$

The above equations can be calculated iteratively by starting with $C_0 = 1$, and the ground state energy solution E_0 can be found by solving the cutoff equation $C_{m+1} = 0$. We show in Fig. 14 the solution of ground state energy per site E_0/L as a function of cutoff excitation number m for system length $L = 200, 400, 800, 1600$.

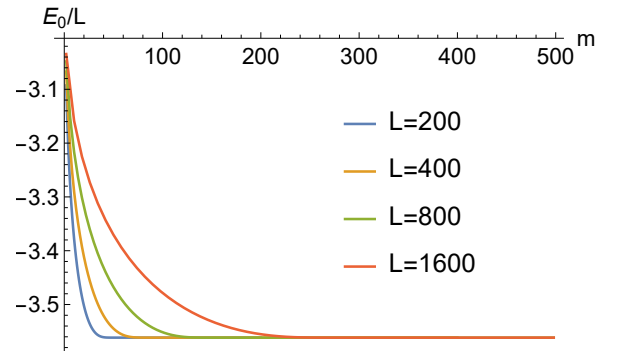


FIG. 14. The ground state energy E_0/L of the dimer point as a function of cut-off excitation number m at the limit of free bond excitations. The energy converges to $E_0/L \approx -3.56155$ and provides an upper limit for the ground state energy of the dimer point.

As illustrated, the convergent energy is well described by cutoff excitation number $m \ll L$, which reflects the fact that the two-bond excitations are in fact dilute, and thus it is reasonable to assume that these excitations are

non-interacting. Finally, we find the energy converges to $E_0/L \approx -3.56155$, which is very close to our DMRG results with $E_0/L \approx -3.594$, and provides an upper limit for this dimer point.

-
- [1] F. D. M. Haldane, Phys. Lett. A **93**, 464 (1983); Phys. Rev. Lett. **50**, 1153 (1983).
- [2] I. Affleck, T. Kennedy, E. H. Lieb, and H. Tasaki, Phys. Rev. Lett. **59**, 799 (1987).
- [3] I. Affleck, J. Phys.: Condens. Matter **1**, 3047 (1989).
- [4] Z. Gu and X. Wen, Phys. Rev. B **80**, 155131 (2009).
- [5] F. Pollmann, A. M. Turner, E. Berg, and M. Oshikawa, Phys. Rev. B **81**, 064439 (2010).
- [6] F. Pollmann, E. Berg, A. M. Turner, and M. Oshikawa, Phys. Rev. B **85**, 075125 (2012).
- [7] M. Lajkó, K. Wamer, F. Mila, and I. Affleck, Nucl. Phys. B **924**, 508 (2017).
- [8] Y. Yao, C. T. Hsieh, and M. Oshikawa, Phys. Rev. Lett. **123**, 180201 (2019).
- [9] K. Wamer, M. Lajkó, F. Mila, and I. Affleck, Nucl. Phys. B **952**, 114932 (2020).
- [10] M. Greiter, S. Rachel, and D. Schuricht, Phys. Rev. B **75**, 060401(R) (2007).
- [11] M. Greiter and S. Rachel, Phys. Rev. B **75**, 184441 (2007).
- [12] S. Rachel, R. Thomale, M. Führinger, P. Schmitteckert, and M. Greiter, Phys. Rev. B **80**, 180420(R) (2009).
- [13] K. Wamer and I. Affleck, Phys. Rev. B **101**, 245143 (2020).
- [14] K. Duivenvoorden and T. Quella, Phys. Rev. B **86**, 235142 (2012).
- [15] K. Duivenvoorden and T. Quella, Phys. Rev. B **87**, 125145 (2013).
- [16] K. Duivenvoorden and T. Quella, Phys. Rev. B **88**, 125115 (2013).
- [17] D. Else, S. Bartlett, and A. Doherty, Phys. Rev. B **88**, 085114 (2013).
- [18] T. Morimoto, H. Ueda, T. Momoi, and A. Furusaki, Phys. Rev. B **90**, 235111 (2014).
- [19] I. Affleck, D. Bykov, and K. Wamer, Phys. Rep. **953**, 1 (2022).
- [20] S. Gozel, P. Nataf, and F. Mila, Phys. Rev. Lett. **125**, 057202 (2020).
- [21] P. Fromholz and P. Lecheminant, Phys. Rev. B **102**, 094410 (2020).
- [22] L. Devos, L. Vanderstraeten, and F. Verstraete, Phys. Rev. B **106**, 155103 (2022).
- [23] K. Wamer, F. H. Kim, M. Lajkó, F. Mila, and I. Affleck, Phys. Rev. B **100**, 115114 (2019).
- [24] S. Rachel, D. Schuricht, B. Scharfenberger, R. Thomale, and M. Greiter, J. Phys.: Conf. Ser. **200**, 022049 (2010).
- [25] A. Roy and T. Quella, Phys. Rev. B **97**, 155148 (2018).
- [26] S. Gozel, D. Poilblanc, I. Affleck, and F. Mila, Nucl. Phys. B **945**, 114663 (2019).
- [27] H. Katsura, T. Hirano, and V. E. Korepin, J. Phys. A: Math. Theor. **41**, 135304 (2008).
- [28] J. Xu, Q. Gu, and E. J. Mueller, Phys. Rev. Lett. **120**, 085301 (2018).
- [29] H. Yang, H. Nakano, and H. Katsura, Phys. Rev. Research **3**, 023210 (2021).
- [30] M. A. Cazalilla and A. M. Rey, Rep. Prog. Phys. **77**, 124401 (2014).
- [31] H. Nonne, M. Moliner, S. Capponi, P. Lecheminant, and K. Totsuka, Europhys. Lett. **102**, 37008 (2013).
- [32] V. Bois, S. Capponi, P. Lecheminant, M. Moliner, and K. Totsuka, Phys. Rev. B **91**, 075121 (2015).
- [33] H. Ueda, T. Morimoto, and T. Momoi, Phys. Rev. B **98**, 045128 (2018).
- [34] P. Fromholz, S. Capponi, P. Lecheminant, D. J. Papoular, and K. Totsuka, Phys. Rev. B **99**, 054414 (2019).
- [35] A. Auerbach, *Interacting Electrons and Quantum Magnetism* (Springer, Berlin, 1998).
- [36] M. Mathur and D. Sen, J. Math. Phys. **42**, 4181 (2001).
- [37] S. Chaturvedi and N. Mukunda, J. Math. Phys. **43**, 5262 (2002).
- [38] R. Anishetty, M. Mathur, and I. Raychowdhury, J. Math. Phys. **50**, 053503 (2009).
- [39] Y. Kawaguchi and M. Ueda, Phys. Rep. **520**, 253 (2012).
- [40] H. Yang and H. Katsura, Phys. Rev. Lett. **122**, 053401 (2019).
- [41] M. Theis, G. Thalhammer, K. Winkler, M. Hellwig, G. Ruff, R. Grimm, and J. Hecker Denschlag, Phys. Rev. Lett. **93**, 123001 (2004).
- [42] C. D. Hamley, E. M. Bookjans, G. Behin-Aein, P. Ahmadi, and M. S. Chapman, Phys. Rev. A **79**, 023401 (2009).
- [43] D. J. Papoular, G. V. Shlyapnikov, and J. Dalibard, Phys. Rev. A **81**, 041603(R) (2010).
- [44] G. Grynberg and C. Robilliard, Phys. Rep. **355**, 335 (2001).
- [45] J. Ruostekoski, G. V. Dunne, and J. Javanainen, Phys. Rev. Lett. **88**, 180401 (2002).
- [46] D. McKay and B. DeMarco, New J. Phys. **12**, 055013 (2010).
- [47] D. Jaksch and P. Zoller, New J. Phys. **5**, 56 (2003).
- [48] M. Aidelsburger, M. Atala, S. Nascimbène, S. Trotzky, Y. A. Chen, and I. Bloch, Phys. Rev. Lett. **107**, 255301 (2011).
- [49] H. Miyake, G. A. Siviloglou, C. J. Kennedy, W. C. Burton, and W. Ketterle, Phys. Rev. Lett. **111**, 185302 (2013).
- [50] M. Cohen. and T. Feldmann, J. Phys. B: At. Mol. Phys. **15**, 2563 (1982).
- [51] W. Greiner and B. Müller, *Quantum Mechanics: Symmetries* (Springer, Berlin, 1994).
- [52] H. Georgi, *Lie Algebras in Particle Physics* (Westview, Boulder, 1999).
- [53] S. Capponi, P. Fromholz, P. Lecheminant, and K. Totsuka, Phys. Rev. B **101**, 195121 (2020).
- [54] H. Ott, Rep. Prog. Phys. **79**, 054401 (2016).
- [55] W. S. Bakr, J. I. Gillen, A. Peng, S. Fölling, and M. Greiner, Nature **462**, 74 (2009).
- [56] W. S. Bakr, A. Peng, M. E. Tai, R. Ma, J. Simon, J. I. Gillen, S. Fölling, L. Pollet, and M. Greiner, Science **329**, 547 (2010).

- [57] J. F. Sherson, C. Weitenberg, M. Endres, M. Cheneau, I. Bloch, and S. Kuhr, *Nature* **467**, 68 (2010).
- [58] M. Endres, M. Cheneau, T. Fukuhara, C. Weitenberg, P. Schauß, C. Gross, L. Mazza, M. C. Bañuls, L. Pollet, I. Bloch, and S. Kuhr, *Science* **334**, 200 (2011).
- [59] P. Sompert, S. Hirthe, D. Bourgund, T. Chalopin, J. Bibo, J. Koepsell, P. Bojović, R. Verresen, F. Pollmann, G. Salomon, C. Gross, T. A. Hilker, and I. Bloch, *Nature* **606**, 484 (2022).
- [60] H. Pichler, G. Zhu, A. Seif, P. Zoller, M. Hafezi, *Phys. Rev. X* **6**, 041033 (2016).
- [61] C. Bardyn, L. Wawer, A. Altland, M. Fleischhauer, and S. Diehl, *Phys. Rev. X* **8**, 011035 (2018).
- [62] P. Mognini and N. Cooper, *Phys. Rev. Res.* **5**, 023004 (2023).